CA23125 - The mETamaterial foRmalism approach to recognize cAncer (TETRA)
Working Group 3, 2026

ELECTROMAGNETIC CHARACTERIZATION OF TESTICULAR TISSUE AND ANTENNA DESIGN FOR EARLY-STAGE CANCER DETECTION. PART 3.2. COLLECTION OF MEASURED PARAMETERS FOR DIFFERENT BIOMATERIALS POSSESSING HIGH DEGREE OF DISORDER.

FIKRET ALPAY TEKSEN

Abstract

Biological tissues are highly disordered composites: cells, membranes, extracellular fluid and fibrous structures are arranged randomly on many length scales. Their macroscopic electromagnetic response is an effective property of this disorder. This report collects the electromagnetic and structural parameters of the biomaterials involved in microwave detection of testicular cancer, as an input dataset for the homogenisation methods developed in the TETRA Action (Part 2.1). The collection covers five tissue classes of the human scrotum and testis (scrotal skin, tunica albuginea, testicular parenchyma, epididymis/rete testis and malignant tumour), two tissue-mimicking phantom liquids characterised from 1 to 20 GHz, the geometric parameters of the tissue layers and inclusions, and the materials of the sensing chain. At 2.45 GHz the tumour-mimicking phantom has $\varepsilon' = 64.5$ against $\varepsilon' = 55.8$ for healthy parenchyma, a contrast of 15.6%, and the assigned conductivities differ by 35.9%. From these values, loss tangents, penetration depths, wavelengths in tissue and Maxwell Garnett effective permittivities of the tumour-bearing testis are derived. The homogenised permittivity of the whole testis changes by less than 1% for tumours of 6–12 mm. This explains why local near-field sensing, and not bulk averaging, is needed for early detection. The parameter set was used to design a meander-line reflection sensor and an antipodal Vivaldi array, which were tested on a 3D-printed phantom. The data were collected during a Short-Term Scientific Mission (STSM) that included clinical measurements on freshly excised human testicular tissue.

1. INTRODUCTION

Testicular cancer is the most frequent solid malignancy in young men aged roughly 15–40 years. Its incidence has increased in many countries, with the highest rates reported in Northern and Western Europe [30, 2]. Cure rates are excellent when the disease is detected at an early, organ-confined stage [4]. Diagnosis relies on palpation, high-frequency scrotal ultrasonography and serum tumour

markers, and histology is obtained only after radical inguinal orchiectomy, because biopsy of a testicular mass risks seeding tumour cells [25, 23]. A cheap, non-ionising technique that can be used frequently could flag suspicious changes earlier.

Microwave sensing uses the contrast in complex permittivity between tissues [3, 24]. This contrast comes from the microstructure. Water content, ionic concentration, membrane charging and the random packing of cells all enter the measured permittivity [7, 8, 9]. From the point of view of the theory of composites, a tissue is a random multi-phase medium, and its permittivity is an effective constant obtained by homogenisation. The TETRA Action builds on this view: it treats tissue as an effective (meta)material and recognises cancer from changes in the effective constants [13]. Part 2.1 of this series develops homogenisation methods for highly disordered structures [21]. These methods need measured constants of the phases as input.

For the breast, large studies on surgical specimens provide such constants for normal, benign and malignant tissue [19, 20], and cellular-level signatures have also been measured [14]. For the testis, the data used in simulations come from general compilations [7, 16], which rely on a small number of animal and post-mortem samples. The present part closes part of this gap. It collects the parameters measured or adopted in our work on testicular cancer sensing [29] and adds derived quantities that are needed by both homogenisation models and antenna designers.

The data were gathered during an STSM carried out at the Department of Urology, Kahramanmaraş Sütçü İmam University Faculty of Medicine, and at the microwave laboratory of İskenderun Technical University (Türkiye), in collaboration with VILNIUS TECH (Lithuania).

2. Biological tissue as a highly disordered dielectric

The response of a tissue to a time-harmonic field of angular frequency $\omega = 2\pi f$ is described by the complex relative permittivity

$$\varepsilon^*(\omega) = \varepsilon'(\omega) - j\varepsilon''(\omega) = \varepsilon'(\omega) - j\frac{\sigma(\omega)}{\omega\varepsilon_0}, \tag{1}$$

where ε' is the relative permittivity, ε'' the loss factor, σ the effective conductivity and ε_0 the permittivity of vacuum. The loss tangent is $\tan\delta_e = \varepsilon''/\varepsilon'$. In the microwave range, the dominant mechanism is the γ-dispersion of water. Broadband spectra are summarised by the multi-pole Cole–Cole model [5, 9]

$$\varepsilon^*(\omega) = \varepsilon_\infty + \sum_{n=1}^{N} \frac{\Delta\varepsilon_n}{1 + (j\omega\tau_n)^{1-\alpha_n}} + \frac{\sigma_i}{j\omega\varepsilon_0}. \tag{2}$$

The broadening parameters α_n are a direct trace of disorder. A medium with a single relaxation time has $\alpha_n = 0$. A distribution of relaxation times, caused by the random sizes, shapes and environments of the cells, gives $0 < \alpha_n < 1$ [9].

Two derived quantities matter for sensing. The field attenuation constant and penetration depth are

$$\alpha = \omega\sqrt{\frac{\mu_0\varepsilon_0\varepsilon'}{2}}\left[\sqrt{1+\tan^2\delta_e} - 1\right]^{1/2}, \qquad \delta = \frac{1}{\alpha}, \tag{3}$$

and the wavelength in the tissue is approximately $\lambda_t = c/(f\sqrt{\varepsilon'})$.

A tumour inside the parenchyma is an inclusion in a host. For a dilute concentration f_v of spherical inclusions with permittivity ε_i in a host with permittivity ε_m, the Maxwell Garnett formula

gives the effective permittivity [10, 27]

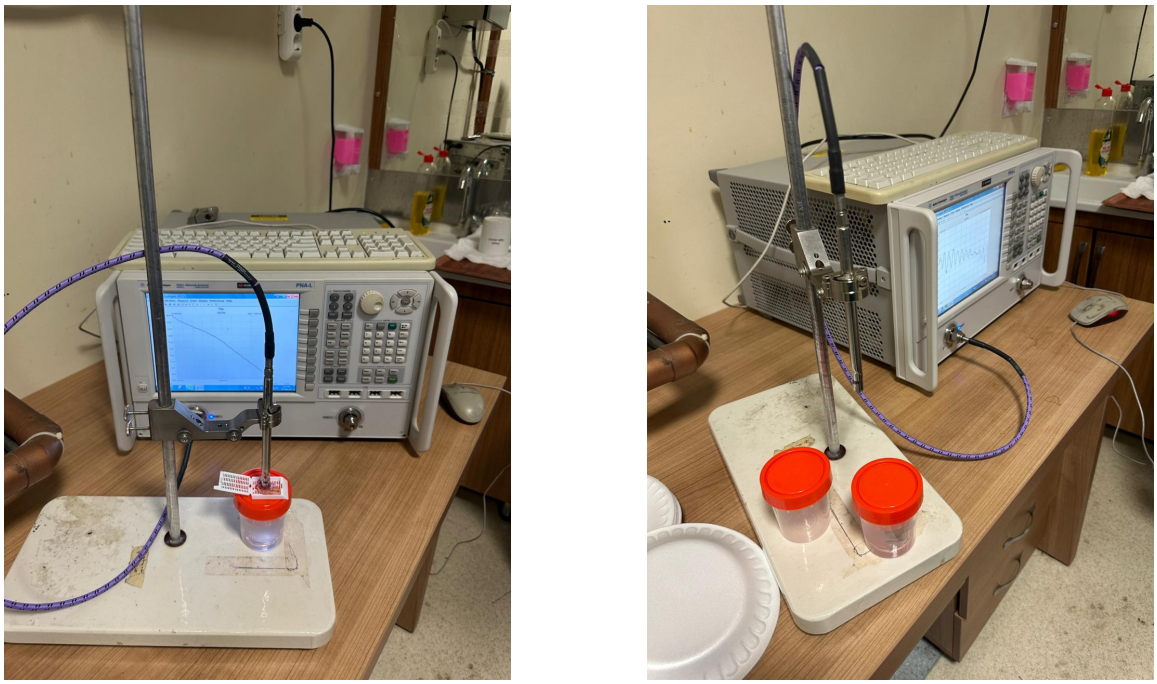
$$\varepsilon_{\mathrm{eff}} = \varepsilon_m \frac{1+2f_v\beta}{1-f_v\beta}, \qquad \beta = \frac{\varepsilon_i-\varepsilon_m}{\varepsilon_i+2\varepsilon_m}. \tag{4}$$

Equation (4) is the 3D counterpart of the first-order formula analysed in Part 2.1 [21]. It is exact only to first order in f_v, and it ignores the positions of the inclusions. Part 2.1 shows how higher-order terms that depend on the spatial arrangement can be obtained. Here, Eq. (4) is used only to estimate the order of magnitude of the effect of a tumour on the bulk response (Section 4.4).

3. Measurement framework

3.1. **Clinical framework and tissue measurements.** Ethical committee approval and official access to the hospital and the operating theatre were obtained before the clinical phase. The dielectric measurements are non-destructive and take only a few minutes. They do not interfere with the routine histopathological work-up. Data were recorded in pseudonymised form, and no identifiable patient information is shown in this report.

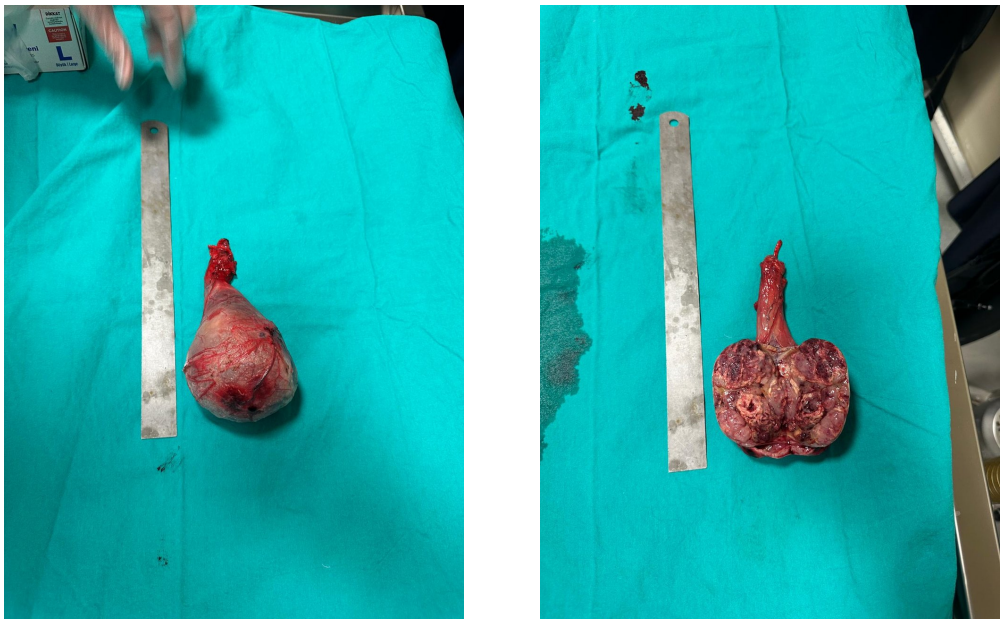
The measurement station installed at the hospital is shown in Figure 1. A slim open-ended coaxial probe was fixed on a rigid stand and clamp. This kept probe height and contact pressure constant during each measurement. The probe was connected to the VNA through a phase-stable cable, held still after calibration to limit phase drift.



(A) (B)

Figure 1. Dielectric measurement station at the host hospital. (a) VNA with the open-ended coaxial probe on a rigid stand; the specimen container sits directly under the probe tip, and the probe is lowered onto the tissue without moving the cable. (b) The same station with two specimen containers, for measuring healthy and tumorous samples from the same patient one after the other under one calibration.

Two radical inguinal orchiectomies were attended. Immediately after excision, the specimens were brought to the station (Figure 2). Samples were taken from the macroscopically tumorous region and from macroscopically healthy tissue. The bisected specimen in Figure 2(b) shows the degree of disorder in a real tumour: the cut surface is lobulated and heterogeneous, with regions of different texture and colour side by side. The measurement of tissue fragments is shown in Figure 3.



(A) (B)

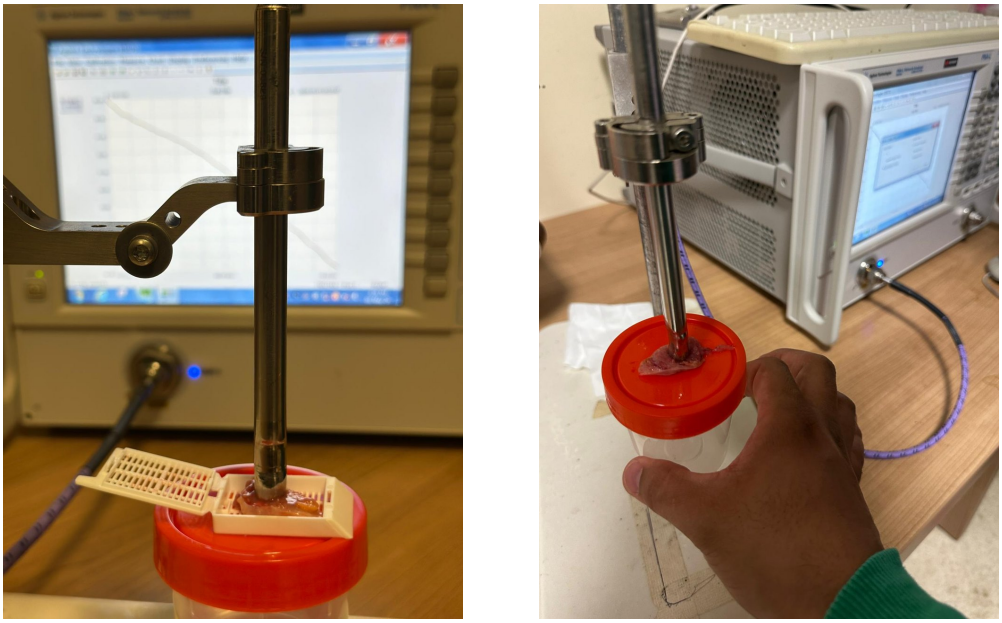
FIGURE 2. Radical inguinal orchiectomy specimens (metal ruler for scale). (a) Intact testis with the spermatic cord. (b) Bisected specimen: the tumour is lobulated and strongly heterogeneous, a macroscopic example of the disorder that the effective parameters must represent.

The clinical spectra are being post-processed by Cole–Cole fitting (2) and will be added to this collection as a separate dataset. The values reported in Section 4 are those measured on tissue-mimicking phantoms and those adopted for the numerical model in [29].

3.2. **Open-ended coaxial probe method.** All dielectric data were measured with an Agilent 85070 open-ended slim-form coaxial probe connected to an Agilent PNA-L vector network analyser [29]. The probe measures the reflection coefficient Γ at its aperture. In the lumped-element model of [28],

$$\Gamma(\omega) = \frac{1 - Z_0 Y(\omega)}{1 + Z_0 Y(\omega)}, \qquad Y(\omega) = j\omega C_f + j\omega C_0\, \varepsilon^*(\omega), \tag{5}$$

where C_f is the fringing capacitance inside the probe, C_0 the capacitance in the sample and Z_0 the characteristic impedance. Calibration used open (air), short and deionised water standards. The main confounders are contact pressure, temperature, air gaps, cable movement and heterogeneity within the sensing volume [12, 26]. The last one is critical for disordered materials: the probe senses only a small volume near its aperture, so a measurement on heterogeneous tissue is itself a local average whose value depends on where the probe is placed [26].



(A) (B)

FIGURE 3. Ex vivo measurement of freshly excised testicular tissue. (a) Probe aperture in contact with a tissue fragment in a histology cassette while the VNA records the spectrum. (b) Probe lowered onto a tissue sample on the lid of the specimen container.

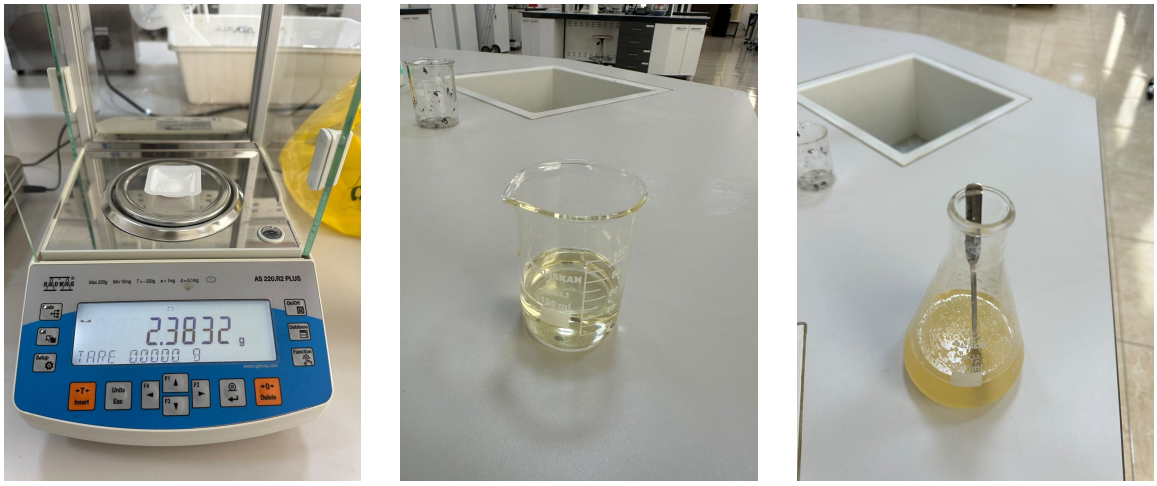
3.3. **Tissue-mimicking phantom materials.** Two phantom liquids were formulated: one for healthy testicular parenchyma and one for the malignant tumour. They consist of deionised water, the non-ionic surfactant Triton X-100 to lower the permittivity, and analytical-grade sodium chloride to set the conductivity [29]. This class of recipe is established for microwave phantoms [18, 22, 17]. Each ingredient was weighed on a Radwag AS 220.R2 PLUS analytical balance with 0.1 mg resolution (Figure 4).

The liquids were measured at a stabilised temperature of 22 °C by immersing the probe (Figure 5). The same probe and calibration were used for tissue and phantoms, so both datasets share one measurement chain.

A bilateral scrotal shell was 3D printed directly from the CAD geometry of the numerical model and filled with the phantom liquids (Figure 6). A healthy pair and a tumour-bearing pair were prepared.

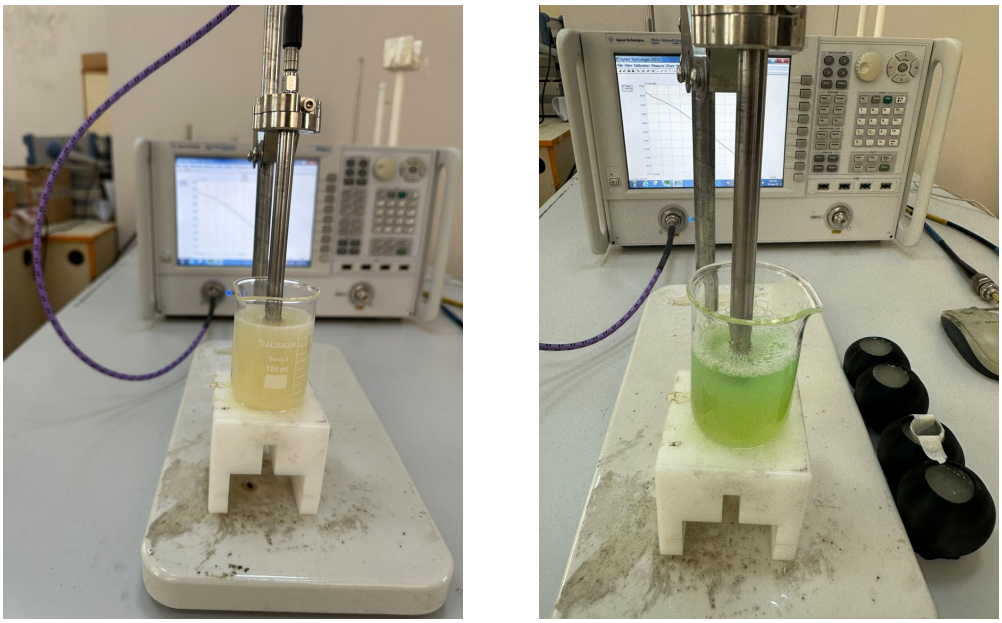
4. COLLECTED PARAMETERS

4.1. **Dielectric parameters at 2.45 GHz.** Table 1 collects the dielectric parameters of the five tissue classes at 2.45 GHz. The permittivities of the parenchyma and the tumour were measured on the phantom liquids. The values for skin, tunica albuginea and epididymis/rete testis, and all conductivities, are those adopted for the numerical model in [29], in agreement with [8, 16]. The columns ε'', $\tan\delta_e$, δ and λ_t were computed here from Eqs. (1) and (3) with $\omega\varepsilon_0 = 0.1363$ S/m.



(A) (B) (C)

FIGURE 4. Preparation of the phantom liquids. (a) Weighing of an ingredient on the analytical balance (0.1 mg resolution). (b) Water–surfactant base mixture. (c) Mixing until the solution is homogeneous.

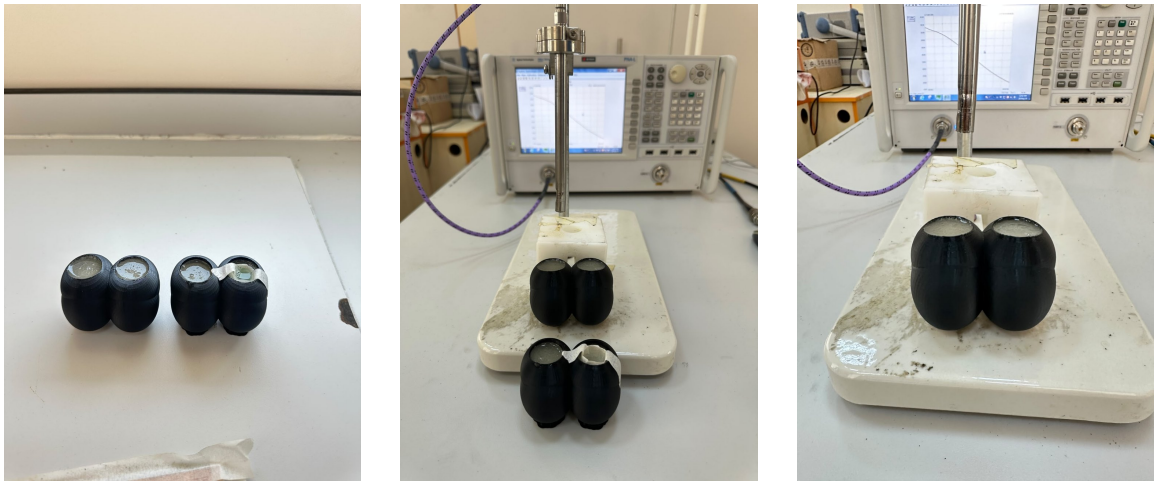


(A) (B)

FIGURE 5. Dielectric characterisation of the phantom liquids with the slim-form probe at 22 °C. (a) Healthy-parenchyma phantom. (b) Malignant-tumour phantom (green); the 3D-printed phantom shells are on the right.

The tumour has the highest permittivity, the highest conductivity and the shortest penetration depth of all tissue classes. The relative contrasts with respect to healthy parenchyma are

$$C_{\varepsilon'} = \frac{\varepsilon'_T - \varepsilon'_H}{\varepsilon'_H} = +15.6\%, \qquad C_{\sigma} = \frac{\sigma_T - \sigma_H}{\sigma_H} = +35.9\%. \tag{6}$$



(A) (B) (C)

FIGURE 6. The 3D-printed bilateral testicular phantom. (a) Healthy and tumour-bearing phantom pairs. (b) Probe check of the filled phantoms on the measurement stand. (c) Close-up of the probe above the filled phantom.

TABLE 1. Dielectric parameters of the testicular tissue classes at 2.45 GHz. ε' and σ from [29]; ε'', $\tan\delta_e$, field penetration depth δ and wavelength in tissue λ_t computed in this work. M = measured on phantom, A = adopted model value.

Tissue class	Geometry	ε'	σ (S/m)	Source	ε''	$\tan\delta_e$	δ (mm)	λ_t (mm)
Scrotal skin	shell, 1.0–2.0 mm	38.0	1.45	A	10.64	0.280	22.8	19.9
Tunica albuginea	shell, 0.6–1.0 mm	44.0	1.60	A	11.74	0.267	22.2	18.4
Testis parenchyma	ellipsoid	55.8	1.95	M (ε')	14.31	0.256	20.5	16.4
Epididymis & rete	tubular mass	52.0	1.82	A	13.35	0.257	21.2	17.0
Malignant tumour	sphere, 6–12 mm	64.5	2.65	M (ε')	19.44	0.301	16.3	15.2

The conductivity contrast is more than twice the permittivity contrast, so loss-sensitive quantities such as the depth of an S_{11} resonance carry useful information in addition to the resonance frequency.

4.2. **Broadband spectra of the phantom liquids.** The measured ε' spectra of the two phantom liquids from 1 to 20 GHz are shown in Figure 7. Both decrease monotonically with frequency, as expected for the γ-dispersion of water. The tumour phantom stays above the parenchyma phantom over the whole band, with $\Delta\varepsilon' \approx 8.7$ at 2.45 GHz [29]. The roughly parallel curves show that the contrast does not depend on a narrow frequency window, which leaves freedom in the choice of the sensing band.

4.3. **Geometric and structural parameters.** The disorder of the testis is represented in the model at two levels: a layered macro-structure and internal micro-structures. Table 2 collects the geometric parameters, and Figure 8 shows the anatomical model. The volume fraction f_v of a single tumour was computed here from the ellipsoid volume $V = \frac{4}{3}\pi \cdot 22.5 \cdot 15 \cdot 12.5 \approx 17\,671\ \mathrm{mm}^3$.

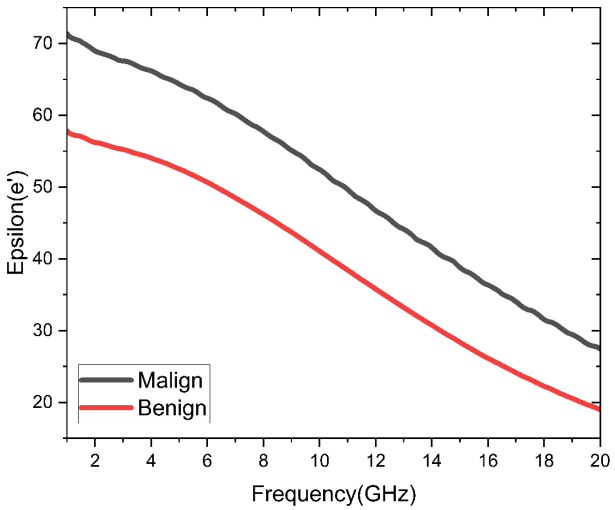


FIGURE 7. Measured real permittivity ε' of the malignant (Malign) and healthy-parenchyma (Benign) phantom liquids from 1 to 20 GHz, measured with the slim-form coaxial probe at 22 °C [29].

TABLE 2. Geometric parameters of the testicular model [29] and the derived tumour volume fraction.

Parameter	Value	Note
Testis (prolate ellipsoid)	$45 \times 30 \times 25$ mm	length × width × thickness
Tunica albuginea / vaginalis	0.6–1.0 mm	conformal shell
Scrotal skin	1.0–2.0 mm (model: 1.50 mm)	antenna interface
Internal structures	epididymis, rete testis, efferent ductules, seminiferous tubules	micro-anatomical heterogeneity
Tumour diameter	6.0–12.0 mm	spherical inclusion
Tumour volume fraction f_v	0.0064 (6 mm) – 0.0512 (12 mm)	computed in this work
Clinical scenarios	single, bilateral, bilateral 1.5× volume, multi-focal	simulated in [29]

4.4. **Effective-medium estimate.** Table 3 gives the Maxwell Garnett effective permittivity (4) of a testis that contains one tumour, using the complex values of Table 1: $\varepsilon_m = 55.8 - j14.31$ and $\varepsilon_i = 64.5 - j19.44$, which give $\beta = 0.0534 - j0.0146$.

Even a 12 mm tumour changes the homogenised permittivity of the whole organ by less than 1%. A sensor that averages over the entire testis would therefore see almost nothing. The local contrast, however, is 15.6% in ε' and 35.9% in σ. Early detection must therefore rely on near-field sensing, in which the antenna probes a volume of the order of the penetration depth ($\approx$ 16–23 mm, Table 1), comparable to the tumour depth. The first-order formula (4) also ignores the position of

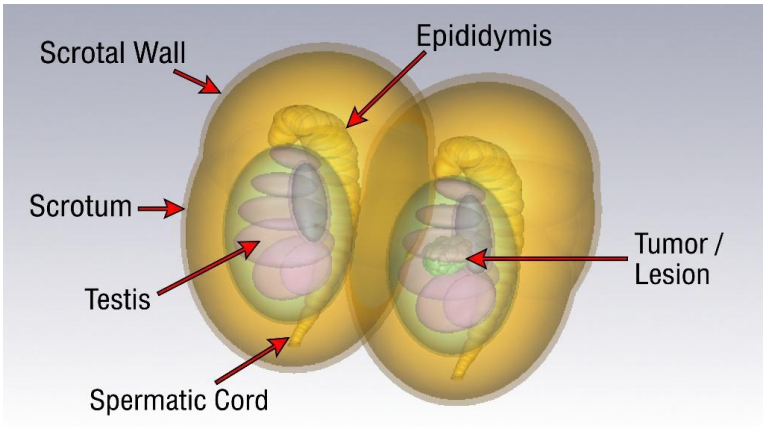


FIGURE 8. Anatomical 3D model of the bilateral testis in CST Microwave Studio with scrotal wall, scrotum, testis, epididymis and spermatic cord; the spherical tumour inclusion (green) is embedded in the right parenchyma [29].

TABLE 3. Maxwell Garnett effective parameters of the tumour-bearing testis at 2.45 GHz (computed in this work).

Tumour diameter (mm)	f_v	$\varepsilon'_{\mathrm{eff}}$	σ_{eff} (S/m)	Change of ε'
6	0.0064	55.85	1.954	+0.10%
8	0.0152	55.93	1.960	+0.23%
10	0.0296	56.05	1.969	+0.44%
12	0.0512	56.23	1.983	+0.76%

the inclusion. The higher-order, position-dependent corrections of Part 2.1 [21] are the natural next step for describing multi-focal tumours, where the arrangement of several inclusions matters.

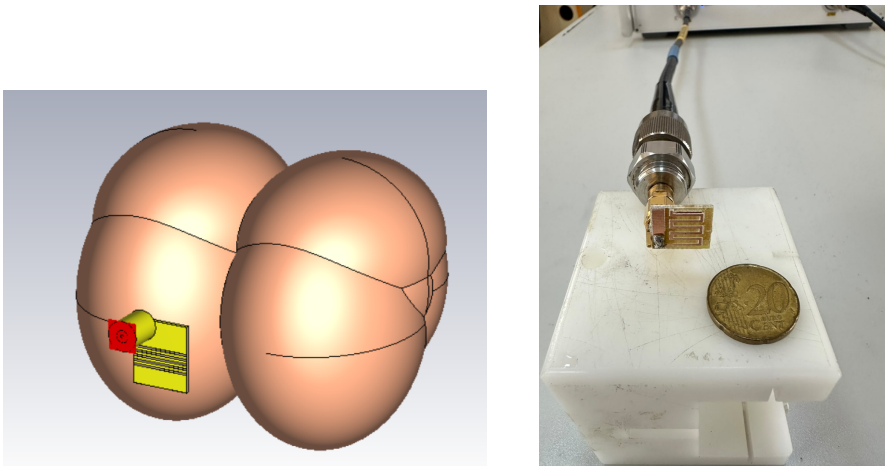
4.5. **Materials of the sensing chain.** Table 4 collects the parameters of the engineered materials in the sensing chain. They are needed to reproduce the measurements and the simulations.

TABLE 4. Materials and dimensions of the meander-line sensor [29].

Item	Parameter	Value
Substrate (FR-4, double-sided)	ε_r, $\tan\delta$, thickness h	4.4, 0.02, 1.52 mm
Substrate size	$L_{sub} \times W_{sub}$	18.0×16.0 mm
Microstrip feed	width W_f, impedance	2.90 mm, 50 Ω
Meander line	width W_m / spacing S_m	0.80 mm / 0.80 mm
Meander resonator	length L_m, number of turns N	10.5 mm, 4

5. Use of the parameter set in sensor design

5.1. **Meander-line reflection sensor.** The parameter set of Tables 1–4 was used in CST Microwave Studio to design a compact meander-line sensor for the 1–4 GHz band [29]. The band is a compromise. Below about 1 GHz the resolution is too coarse for sub-centimetre tumours. Above 3–4 GHz the attenuation in water-rich tissue limits the sensing depth, in line with the penetration depths of Table 1. The sensor touches the scrotal boundary of the model (Figure 9), so its input impedance follows the dielectric loading of its near field.



(A) (B)

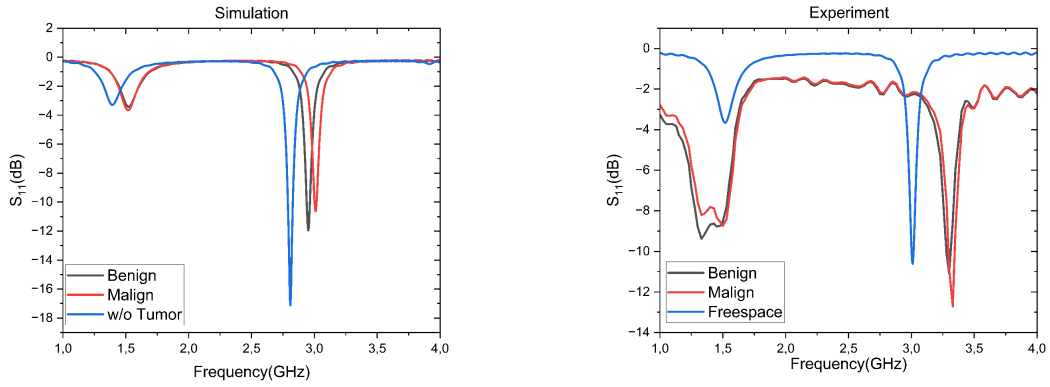
Figure 9. Meander-line reflection sensor. (a) CST simulation set-up with the sensor in direct contact with the scrotal boundary of the bilateral model [29]. (b) Fabricated prototype on 1.52 mm FR-4 with a 20-euro-cent coin for scale.

Table 5 collects the reflection results reported in [29], and Figure 10 shows the spectra.

Table 5. Resonance parameters of the meander-line sensor [29].

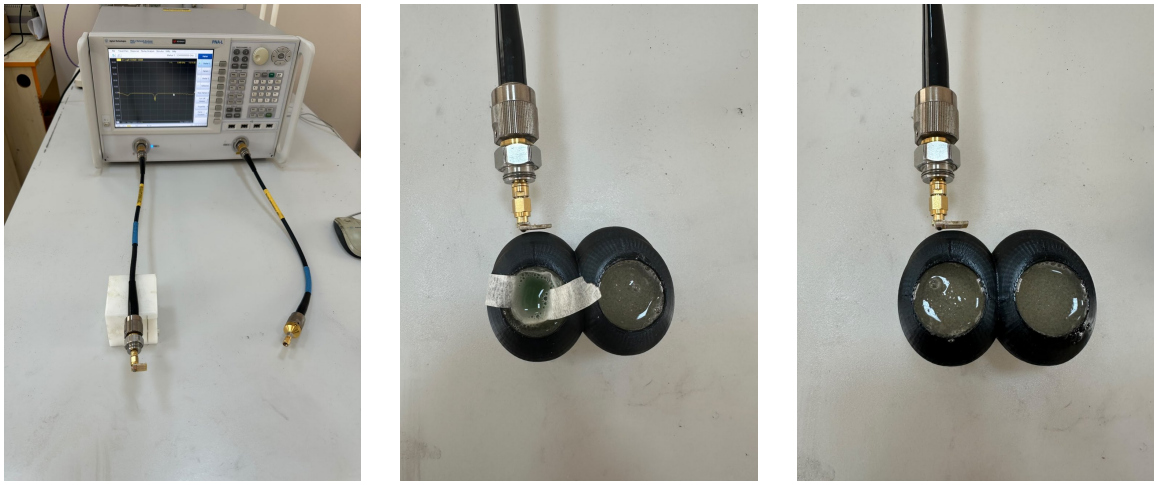
Condition	Data	Resonance (GHz)	$\lvert S_{11}\rvert$ (dB)
Free space	simulation	2.81	−17.1
Free space	measurement	3.01	−10.6
Healthy testis model	simulation	2.96	−12.0
Tumour-bearing model	simulation	–	−10.7
Healthy phantom	measurement	3.31	−11.2
Tumour-bearing phantom	measurement	≈ 3.3	−12.8

The 200 MHz shift between simulated and measured free-space resonances is attributed to etching tolerances, the dispersion of FR-4 and connector parasitics [29]. On the phantom, the tumour deepens the resonance from −11.2 to −12.8 dB ($\Delta\lvert S_{11}\rvert = 1.6$ dB) and changes the absorption in the 1.3–1.5 GHz band. The large conductivity contrast of Eq. (6) is consistent with a change dominated by the resonance depth rather than by its frequency. The measurement set-up on the phantom is shown in Figure 11.



(A) (B)

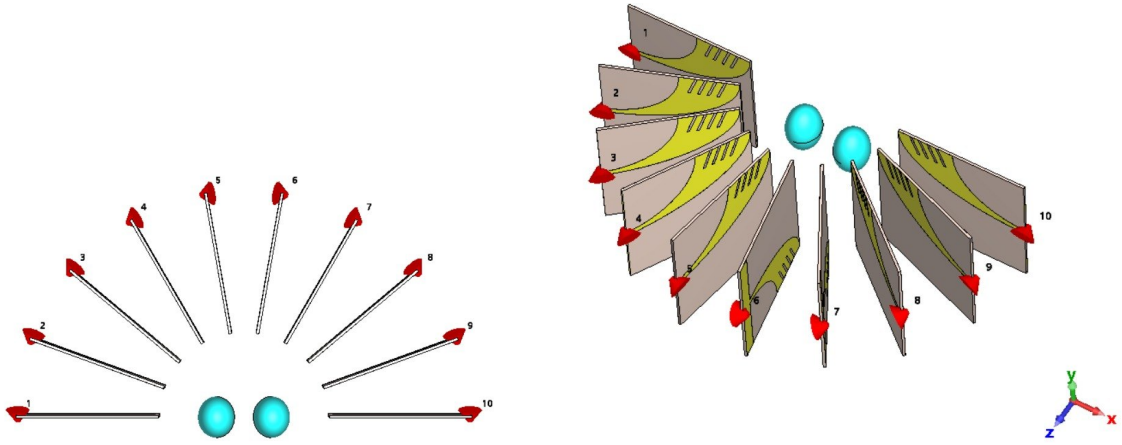
FIGURE 10. Reflection coefficient of the meander-line sensor from 1 to 4 GHz [29]. (a) Simulation: free space (w/o Tumor), healthy model (Benign) and tumour-bearing model (Malign). (b) Measurement on the 3D-printed phantom: free space, healthy phantom and tumour-bearing phantom.



(A) (B) (C)

FIGURE 11. Phantom measurements with the meander-line sensor. (a) Calibrated two-port VNA set-up with the sensor in a PTFE fixture. (b) Sensor on the compartment with the sealed tumour phantom. (c) Sensor on the healthy reference phantom.

5.2. **Antipodal Vivaldi array and conformal sensors.** For imaging, the same tissue parameters were assigned to a ten-element multistatic array of corrugated antipodal Vivaldi antennas [11, 1] arranged on a semicircle around the two testis models (Figure 12). Each element is excited in turn while the others receive, which gives 10×9 transmission channels for detection and image reconstruction [6, 24]. At 2.5 GHz a single element has a simulated directivity of 7.049 dBi, a radiation efficiency of -0.512 dB ($\approx 88.9\%$) and a total efficiency of -0.928 dB ($\approx 80.8\%$) (Figure 13).



(A) (B)

FIGURE 12. Simulation model of the multistatic Vivaldi array. (a) Top view of the ten elements (ports 1–10) around the two testis models. (b) Three-dimensional view.

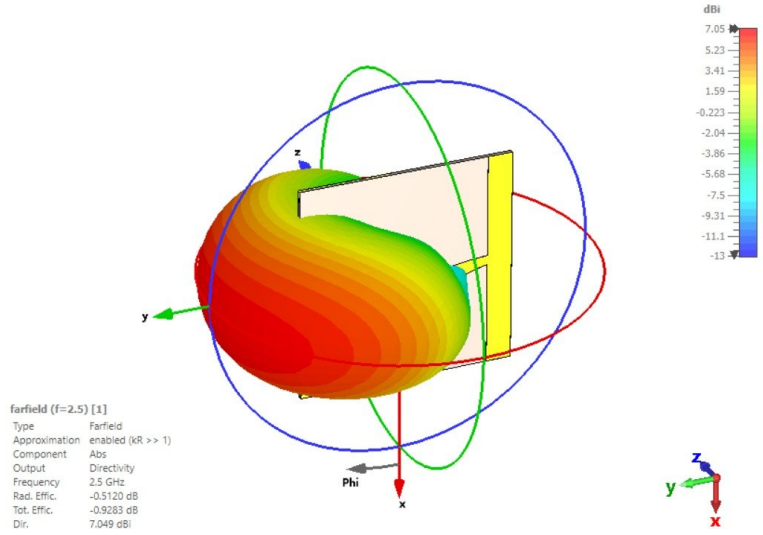


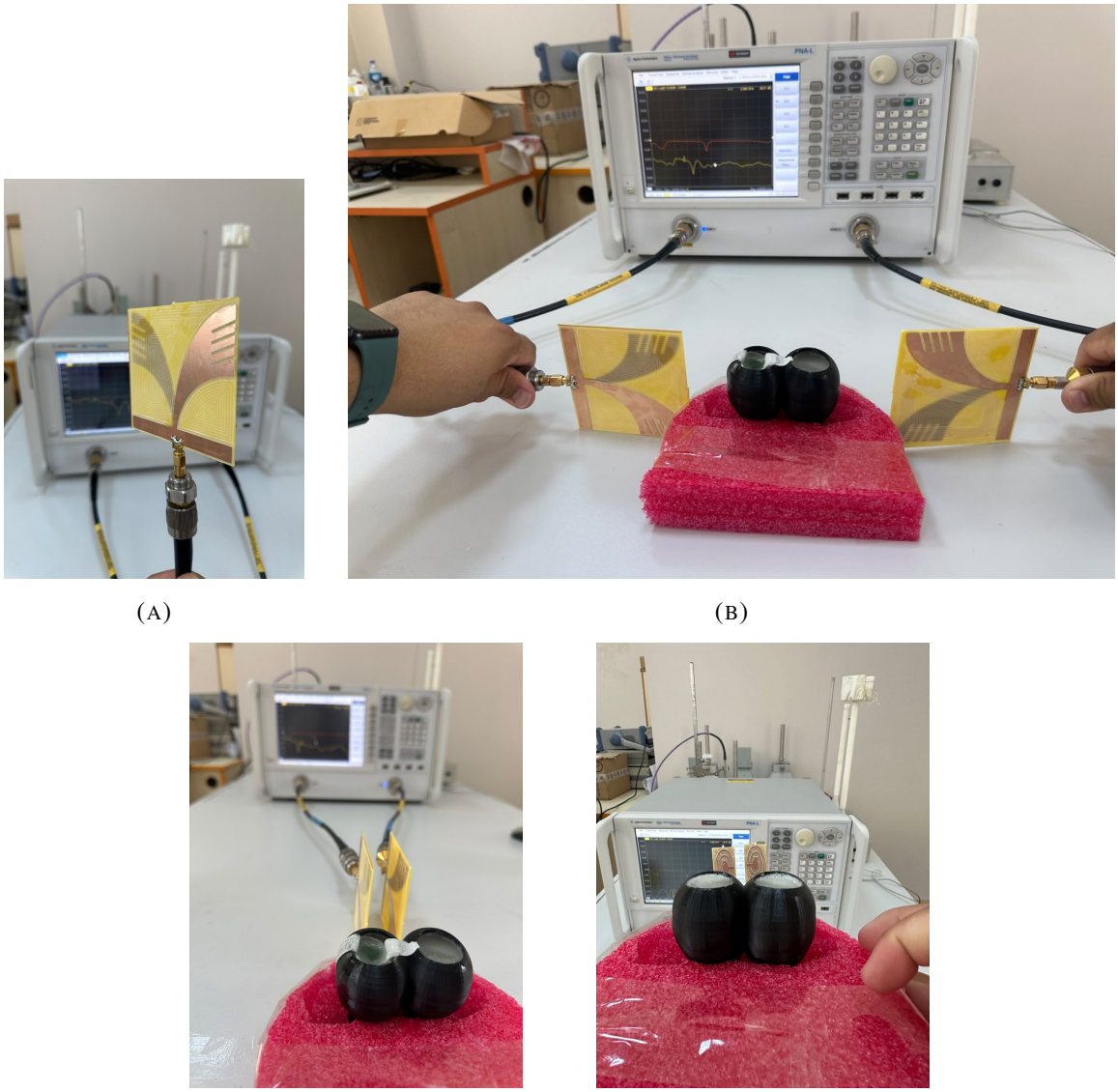
FIGURE 13. Simulated far-field directivity of a single corrugated antipodal Vivaldi element at 2.5 GHz.

Exposure was assessed through the specific absorption rate

$$\mathrm{SAR} = \frac{\sigma\,|\mathbf{E}|^2}{\rho} \quad [\mathrm{W/kg}], \tag{7}$$

using the conductivities of Table 1, against the ICNIRP limit of 2 W/kg averaged over 10 g for the head and torso [15]. Microwave sensing needs only milliwatt-level power, so the system is intended to operate far below this limit.

Prototype Vivaldi antennas were fabricated and used for transmission measurements across the phantom (Figure 14). Compact split-ring-type sensors on a flexible carrier were also prepared for a conformal arrangement around the phantom (Figure 15).



(A) (B)

(C) (D)

FIGURE 14. Vivaldi prototypes and bistatic transmission measurement on the phantom. (a) Fabricated corrugated antipodal Vivaldi antenna connected to the VNA. (b) Two Vivaldi antennas on opposite sides of the phantom, connected to the two VNA ports. (c) Side view. (d) Phantom on the low-permittivity foam holder.



(A) (B)

FIGURE 15. Compact sensors with concentric split-ring patterns. (a) Two sensors next to the filled phantom. (b) Conformal semicircular arrangement on a flexible carrier around the phantom.

6. Conclusions and outlook

This part collected the parameters of the biomaterials involved in microwave detection of testicular cancer. The collection contains the following items:

- permittivity and conductivity at 2.45 GHz for five tissue classes, with derived loss tangents, penetration depths and wavelengths (Table 1);
- broadband (1–20 GHz) permittivity spectra of healthy and tumour phantom liquids (Figure 7);
- the geometric parameters of the layered model and the tumour volume fractions (Table 2);
- Maxwell Garnett effective parameters of the tumour-bearing testis (Table 3);
- the materials and resonance data of the sensing chain (Tables 4 and 5).

The local contrast between tumour and parenchyma is 15.6% in ε' and 35.9% in σ, while the homogenised permittivity of the whole organ changes by less than 1%. Disorder therefore has to be treated at the scale of the sensing volume, not at the scale of the organ.

Next, the Cole–Cole parameters of the clinically measured healthy and tumorous tissue will be added to the collection. The position-dependent homogenisation formulas of Part 2.1 [21] will then be applied to multi-focal tumours. The results will be compiled into a joint manuscript of VILNIUS TECH and the Turkish partner institutions. The collaboration also opens the way to joint applications to Horizon Europe or bilateral funding programmes.

Acknowledgements

This work was supported by COST Action CA23125 *The mETamaterial foRmalism approach to recognize cAncer (TETRA)* through a Short-Term Scientific Mission, funded by COST (European Cooperation in Science and Technology). The author thanks the Department of Urology of Kahramanmaraş Sütçü İmam University Faculty of Medicine, the microwave laboratory of İskenderun Technical University, the co-authors of [29], and the patients who consented to take part in the study.

References

[1] J. Bourqui, M. Okoniewski, and E.C. Fear. Balanced antipodal Vivaldi antenna with dielectric director for near-field microwave imaging. *IEEE Transactions on Antennas and Propagation*, 58(7):2318–2326, 2010.

[2] F. Bray, M. Laversanne, H. Sung, J. Ferlay, R.L. Siegel, I. Soerjomataram, and A. Jemal. Global cancer statistics 2022: GLOBOCAN estimates of incidence and mortality worldwide for 36 cancers in 185 countries. *CA: A Cancer Journal for Clinicians*, 74(3):229–263, 2024.

[3] R. Chandra, H. Zhou, I. Balasingham, and R.M. Narayanan. On the opportunities and challenges in microwave medical sensing and imaging. *IEEE Transactions on Biomedical Engineering*, 62(7):1667–1682, 2015.

[4] L. Cheng, P. Albers, D.M. Berney, D.R. Feldman, G. Daugaard, T. Gilligan, et al. Testicular cancer. *Nature Reviews Disease Primers*, 4(1):29, 2018.

[5] K.S. Cole and R.H. Cole. Dispersion and absorption in dielectrics I. Alternating current characteristics. *The Journal of Chemical Physics*, 9(4):341–351, 1941.

[6] E.C. Fear, X. Li, S.C. Hagness, and M.A. Stuchly. Confocal microwave imaging for breast cancer detection: localization of tumors in three dimensions. *IEEE Transactions on Biomedical Engineering*, 49(8):812–822, 2002.

[7] C. Gabriel, S. Gabriel, and E. Corthout. The dielectric properties of biological tissues: I. Literature survey. *Physics in Medicine and Biology*, 41(11):2231–2249, 1996.

[8] S. Gabriel, R.W. Lau, and C. Gabriel. The dielectric properties of biological tissues: II. Measurements in the frequency range 10 Hz to 20 GHz. *Physics in Medicine and Biology*, 41(11):2251–2269, 1996.

[9] S. Gabriel, R.W. Lau, and C. Gabriel. The dielectric properties of biological tissues: III. Parametric models for the dielectric spectrum of tissues. *Physics in Medicine and Biology*, 41(11):2271–2293, 1996.

[10] J.C. Maxwell Garnett. Colours in metal glasses and in metallic films. *Philosophical Transactions of the Royal Society of London, Series A*, 203:385–420, 1904.

[11] E. Gazit. Improved design of the Vivaldi antenna. *IEE Proceedings H – Microwaves, Antennas and Propagation*, 135(2):89–92, 1988.

[12] A. La Gioia, E. Porter, I. Merunka, A. Shahzad, S. Salahuddin, M. Jones, and M. O'Halloran. Open-ended coaxial probe technique for dielectric measurement of biological tissues: challenges and common practices. *Diagnostics*, 8(2):40, 2018.

[13] T. Gric, S.G. Sokolovski, N. Navolokin, O. Semyachkina-Glushkovskaya, and E.U. Rafailov. Metamaterial formalism approach for advancing the recognition of glioma areas in brain tissue biopsies. *Optical Materials Express*, 10(7):1607–1615, 2020.

[14] M. Hussein, F. Awwad, D. Jithin, H. El Hasasna, K. Athamneh, and R. Iratni. Breast cancer cells exhibits specific dielectric signature in vitro using the open-ended coaxial probe technique from 200 MHz to 13.6 GHz. *Scientific Reports*, 9:4681, 2019.

[15] International Commission on Non-Ionizing Radiation Protection (ICNIRP). Guidelines for limiting exposure to electromagnetic fields (100 kHz to 300 GHz). *Health Physics*, 118(5):483–524, 2020.

[16] IT'IS Foundation. Tissue properties database, version 4.1. IT'IS Foundation, Zurich, doi:10.13099/VIP21000-04-1, 2022.

[17] N. Joachimowicz, B. Duchêne, C. Conessa, and O. Meyer. Anthropomorphic breast and head phantoms for microwave imaging. *Diagnostics*, 8(4):85, 2018.

[18] M. Lazebnik, E.L. Madsen, G.R. Frank, and S.C. Hagness. Tissue-mimicking phantom materials for narrowband and ultrawideband microwave applications. *Physics in Medicine and Biology*, 50(18):4245–4258, 2005.

[19] M. Lazebnik, D. Popovic, L. McCartney, C.B. Watkins, M.J. Lindstrom, J. Harter, et al. A large-scale study of the ultrawideband microwave dielectric properties of normal, benign and malignant breast tissues obtained from cancer surgeries. *Physics in Medicine and Biology*, 52(20):6093–6115, 2007.

[20] A. Martellosio, M. Pasian, M. Bozzi, L. Perregrini, A. Mazzanti, F. Svelto, et al. Dielectric properties characterization from 0.5 to 50 GHz of breast cancer tissues. *IEEE Transactions on Microwave Theory and Techniques*, 65(3):998–1011, 2017.

[21] V. Mityushev. Mathematical modelling of highly disordered anisotropic structures. Part 2.1. New theories enabling homogenization of disordered metamaterials. COST Action CA23125 (TETRA), Working Group 2 report, 2026.

[22] A.T. Mobashsher and A.M. Abbosh. Artificial human phantoms: human proxy in testing microwave apparatuses that have electromagnetic interaction with the human body. *IEEE Microwave Magazine*, 16(6):42–62, 2015.

[23] C.C. Moreno, W.C. Small, J.C. Camacho, V. Master, N. Kokabi, M. Lewis, M. Hartman, and P.K. Mittal. Testicular tumors: what radiologists need to know – differential diagnosis, staging, and management. *RadioGraphics*, 35(2):400–415, 2015.

[24] N.K. Nikolova. Microwave imaging for breast cancer. *IEEE Microwave Magazine*, 12(7):78–94, 2011.

[25] A. Patrikidou, W. Cazzaniga, D. Berney, J. Boormans, I. de Angst, D. Di Nardo, et al. European Association of Urology guidelines on testicular cancer: 2023 update. *European Urology*, 84(3):289–301, 2023.

[26] E. Porter and M. O'Halloran. Investigation of histology region in dielectric measurements of heterogeneous tissues. *IEEE Transactions on Antennas and Propagation*, 65(10):5541–5552, 2017.

[27] A.H. Sihvola and J.A. Kong. Effective permittivity of dielectric mixtures. *IEEE Transactions on Geoscience and Remote Sensing*, 26(4):420–429, 1988.

[28] M.A. Stuchly and S.S. Stuchly. Coaxial line reflection methods for measuring dielectric properties of biological substances at radio and microwave frequencies – a review. *IEEE Transactions on Instrumentation and Measurement*, 29(3):176–183, 1980.

[29] F.A. Tekşen, T. Gric, M. Metin, S. Altın, F.Ö. Alkurt, M. Erdoğan Alkurt, and M. Karaaslan. Microwave sensing for non-invasive testicular cancer detection: numerical modeling and experimental phantom validation. Manuscript, 2026.

[30] A. Znaor, N.E. Skakkebæk, E. Rajpert-De Meyts, T. Kuliš, M. Laversanne, J. Gurney, et al. Global patterns in testicular cancer incidence and mortality in 2020. *International Journal of Cancer*, 151(5):692–698, 2022.